Oxide-supported carbonates reveal a unique descriptor for catalytic performance in the oxidative coupling of methane (OCM)

Huan Wang[1], Roman Schmack[1], Sergey Sokolov[2], Evgenii V. Kondratenko[2], Aliaksei Mazheika[*3], Ralph Kraehnert*[*1]*

** ralph.kraehnert@tu-berlin.de*

*** alex.mazheika@gmail.com, mazheika@tu-berlin.de*

[1] Institut für Chemie, Technische Universität Berlin, Straße des 17 Juni 124, D-10623 Berlin, Germany
[2] Leibniz-Institut für Katalyse eV, Albert-Einstein-Str. 29A, 18059 Rostock, Germany
[3]BasCat - UniCat BASF JointLab, Technische Universität Berlin, Hardenbergstraße 36, 10623 Berlin, Germany

Abstract

The oxidative coupling of methane (OCM) is a promising reaction for direct conversion of methane to higher hydrocarbons. The reaction can be performed over oxide-based catalysts with very diverse elemental composition. Yet, despite decades of research, no general common structure-activity relationship has been deduced. Our recent statistical meta-analysis across a wide range of catalyst compositions reported in the literature suggested that only the catalysts combining thermodynamically stable (under reaction conditions) carbonate and thermally stable oxide support exhibit good catalytic performance. Guided by these findings we explore now experimentally correlations between descriptors for structure, stability and decomposition behavior of supported metal carbonates vs. the materials' respective performance in OCM catalysis. In this study, carbonates of Rb, Cs and Mg were supported on oxides of Sm, Y, Gd, Ce, Sr and Ba, tested in OCM and studied by IR spectroscopy and thermal analysis. From the evaluation of six proposed property-descriptors we derive a statistically robust volcano-type correlation between the onset temperature of carbonate decomposition and the C_2 yield, indicating the importance of CO_2 adsorption and surface carbonates in selective methane conversion. Moreover, we discuss mechanisms that can account for the observed property-performance correlation across a wide range of OCM catalysts. Carbonate species are suggested to block highly reactive sites during OCM catalysis, which reduces overoxidation and enables the formation of C_2 products.

Introduction

Natural gas is widely utilized as a feedstock for the production of energy and chemicals, but it is largely located in remote areas. Natural gas comprises up to 90% of methane. A promising way to use CH_4 as a chemical feedstock is the "dream reaction" of catalytic oxidative coupling of methane (OCM), as it offers a direct conversion route towards more easily transportable C_2 products ethane and ethylene [1,2,3]. The main goal is to achieve simultaneously a high CH_4 conversion, high C_2 selectivity and low CO_2 emissions [4,5,6,7]. However, economically viable C_2 yields well above 30% have not been reached yet on a larger scale [8].

Prior studies suggest that the OCM proceeds via a complex reaction network that involves gas-phase reactions coupled to reactions at the catalyst surface [1,2,3,10,11], where adsorbed oxygen species and lattice oxygen can be involved in C-H bond activation. Unfortunately, the required high reaction temperatures (500 to 1000 °C [2]) obstruct many common in-situ analytical tools. Hence, neither the significance of such defects under practical operation conditions nor the extent to which gas phase reactions contribute to C_2 formation has been firmly established.

Since the first report in the early 1980s [9], a multiple of OCM catalysts have been reported. The reaction is catalyzed by a surprisingly wide range of catalyst compositions. However, despite significant research efforts, no generally valid correlation between a catalyst's composition, its structure and its OCM performance has been established yet [12,13,14].

Basicity has been suggested by many researchers to be the most important property that describes a catalyst's performance in OCM. Basicity can be expressed and quantified in different ways, including Lewis acid-base, Brønsted acid-base, Smith scale, [21] optical basicity, [22] or the ionic-covalent parameter [23]. The interaction with CO_2 has been used as a measure of basicity, typically via temperature programmed desorption of CO_2. Prior attempts to find such correlations were either inconclusive or valid only for a small number of catalysts (see e.g. Carreiro et al. [15], Maitra et al. [19], Choudhary et al. [16,17,18], and Sokolovskii et al. [20] as discussed in more detail in SI 1). To the best of our knowledge, no quantitative and universal correlation between basicity and OCM performance has ever been reported.

Zavyalova, Baerns and coworkers proposed a different approach, and assessed possible correlations between catalyst composition and OCM performance using statistical tools [24]. The authors collected a large set of data on OCM (1866 observations from 421 publications) in terms of catalyst composition, reaction conditions and catalyst performance. A subsequent evaluation via e.g. multiway analysis of variance and regression trees indicated chemical elements that show a positive effect on OCM performance. Some of the identified key elements also feature a strong basicity. However, due to the fact that neither basicity nor any other physico-chemical property of the evaluated catalysts could be incorporated into the analysis, no clear property-performance correlations were obtained.

In another study done by Pirro, Thybaut and coworkers a combination of experimental data with kinetic modeling, k-means clustering and statistical analysis was employed, and such descriptors for OCM performance as enthalpy of H-abstraction from CH_4 molecule, O_2 and CH_3 adsorption enthalpies were proposed [25]. They are linked again to basicity of oxygen sites and materials' conductivity. However, obtained relations have only qualitative level. A quantitative relation was proposed by Kumar, Janik et al. applying first-principles calculations for a set of common OCM catalysts [26], yet the proposed regularities were not linked to catalytic performance of real catalysts. In a study of Lim, Ha and coworkers a volcano-like dependence of C_2 selectivity on (computed) CH_3 adsorption energies was derived based on combined experimental and DFT study for doped $SrTiO_3$ catalysts [27]. Obtained C_2 yields in this study also show a similar dependence, which however appeared to be valid only in a narrow range of catalyst composition. Recently, Ohyama et al. approached the search for OCM relations by a combined experimental and ML approach [28]. Using a set of systematically measured performance data, material properties

and compositions suited for low temperature OCM were proposed. Based on that several compositions were proposed, although experimental validation suggest that the distribution of their catalytic activities is similar for all studied materials. In conclusion, no clear universal correlation was revealed yet.

We reported recently a new meta-analysis approach that incorporated descriptors for simple physico-chemical properties of the studied OCM catalysts [29]. Considered descriptors included melting points, Tammann temperatures and decomposition temperatures of the simple oxides as well as the carbonates that can be formed by each metal contained in a given catalyst. Based on the descriptors 1802 catalysts reported in literature were sorted into 10 different groups with distinct physico-chemical properties. Regression analysis indicated a strong correlation between given property groups and their catalytic OCM performance (C_2 yield). Well-performing catalysts comprised at least two components, with one element being able to form a thermodynamically stable carbonate at the temperatures of OCM reaction, and a second element forming a thermally stable (non-sintering) oxide under OCM conditions. C_2 yields improved further if the support oxide was also able to form a carbonate. Thus, carbonate stability appears to be a key parameter in OCM catalysis.

However, the meta-analysis was limited in the availability of sufficient data concerning both properties as well as the performance descriptors. For lack of better options, the property descriptors were computed from the nominal catalyst composition, i.e. the chemical elements contained in each catalyst in combination with knowledge on the properties of monometallic oxides reported in literature. However, this can only approximate the real behavior, since the interplay between catalytically active species and a catalyst support can be highly complex in terms of e.g. metal support interactions or the stabilization / destabilization of a carbonate phase. So far, neither stability nor reactivity of supported carbonates can be comprehensively assessed from either literature data or *ab initio* calculations. As a matter of fact, the functions that have been attributed to carbonates in literature range from deactivation of catalysts [30,31] to promotion of catalytic activity [32]. The OCM performance data reported in literature were often obtained at the reaction conditions that varied significantly between different catalysts, i.e. feed gas composition, temperature and contact time, which makes comparison difficult. Thus, elucidating the role of carbonates in OCM catalysis requires dedicated experiments, both in terms of catalytic performance and material characterization.

Using a design of experiments (DOE) guided by the statistical model obtained in the OCM meta-analysis of Schmack et al. [29] we identified catalyst compositions, reaction conditions and suitable analytical tools to explore quantitative correlations based on experimental data. The rational behind choosing these materials was a combination of (a) covering a reasonably wide range of elements known for some sort of OCM activity, (b) having OCM-relevant (thermally stable) supports, (c) being able to synthesize the catalyst with reasonable effort. The approach is outlined in Scheme 1. In total 21 representative binary catalysts were synthesized and measured in OCM. The catalysts were characterized by scanning electron microscopy, IR spectroscopy, N_2 sorption as well as thermal analysis TGA-MS. From obtained characterization data, the property descriptors of potential interest were formulated and respective numerical values calculated from the experimental data. A subsequent analysis of possible correlations between the property descriptors and the respective catalytic performance revealed a simple volcano-type relationship between C_2 yield and carbonate stability. Only well-performing catalysts show the decomposition of a carbonate near the onset temperature of OCM, whereas too high or too low carbonate stability resulted in lower C_2 yields. This finding represents the first quantitative property-performance correlation that is valid for such a wide range of catalyst compositions. Based on this correlation, we propose a possible mechanistic explanation where carbonates would block the surface for unselective oxidation, and a partially decomposed carbonates provide active sites for selective methane activation.

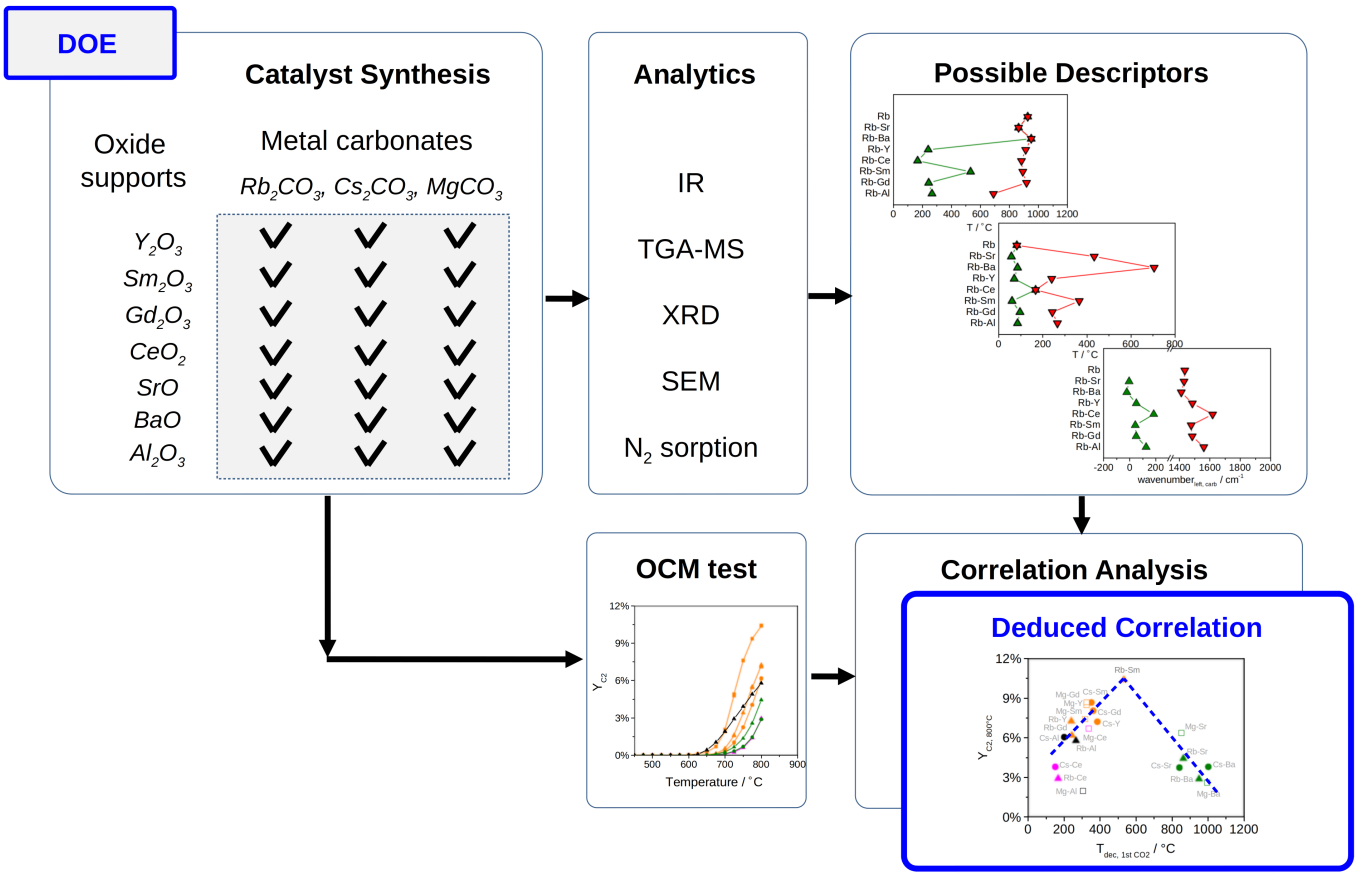

Scheme 1. Approach for the DOE guided search for property performance correlations in OCM. All respective figures appear further in detail in the manuscript.

Catalyst performance in OCM

Catalysts were synthesized by impregnating different oxide supports (SrO, BaO, Y_2O_3, Sm_2O_3, CeO_2, Gd_2O_3, Al_2O_3) with one of the precursors (rubidium carbonate, cesium carbonate or magnesium acetate) thus preparing all possible 21 binary combinations. For more detail see the Method section. The OCM performance of all catalysts was tested in continuous-flow fixed bed reactors at temperatures from 450 °C to 800 °C (25 K steps) using a feed of CH_4 (26%), O_2 (15%) and N_2(59%) and GC analysis. Catalyst characterization included N_2 physisorption, Scanning Electron Microscopy (SEM), energy dispersive X-ray spectroscopy (EDX), X-ray powder diffraction (XRD), FTIR spectroscopy as well as thermogravimetric analysis in Ar flow combined with online mass spectroscopy of the evolved species (TGA-MS). Different numeric property descriptor values were derived from FTIR spectra (band positions) and TGA-MS (temperatures of releasing CO_2 or water). Possible correlations between each property descriptor and each performance descriptor (combined yield of ethane and ethylene at 750°C, $Y_{C2,750°C}$, and 800°C, $Y_{C2,800°C}$) were tested via regression analysis.

All studied catalysts are active in OCM. Table 1 lists the C_2 yields obtained at 750°C ($Y_{C2,750°C}$) as well as 800°C ($Y_{C2,800°C}$). The different catalysts are referred to by the contained elemental combination of supported carbonate and support oxide, where e.g. "Rb-Sr" corresponds to 10 mol% Rb_2CO_3 supported on SrO. A more detailed presentation of the catalytic results is provided in SI2, where methane conversion, oxygen conversion and C_2 yield are listed for each catalyst for the entire temperature range.

In agreement with literature, the onset of product formation is observed between 500 and 600°C, depending on catalyst composition. Both, the support and the supported metal strongly influence the catalytic performance. All catalysts show an increase in Y_{C2} with increasing reaction temperature. For Rb-Al and Cs-Al an early onset of methane conversion is observed whereas C_2 hydrocarbons are formed only above 600°. At typical OCM conditions, i.e. 800°C, the observed methane conversion ranges from 8% (Rb-Ce) to ca. 42% (Rb-Sm, Mg-Gd), and C_2 selectivities range from 6.6% (Mg-Al) to 40.8% (Cs-Ce). C_2 yields between 2.0% (poorly selective Mg-Al) and 10.4% (Rb-Sm) were observed with an average of 5.9%. Thus, the observed performance values and trends are in line with literature results. Moreover, catalysts of different composition demonstrated activity and selectivity in a broad range, which provides the opportunity to explore quantitatively the physico-chemical material properties that control OCM performance.

For Rb_2CO_3 and Cs_2CO_3 on oxides, most of catalysts show similar temperature-dependent trend of CH_4 and O_2 conversion except for Al_2O_3 supported ones, which exhibit significant conversion at fairly low temperature (550 °C). Rb-Sm, Rb-Y and Rb-Gd show higher CH_4 and O_2 conversion than Rb-Ce, Rb-Sr and Rb-Ba at typical OCM temperatures. Their C_2 yields mainly grow with CH_4 conversion. $Mg(OAc)_2$ on oxides show different behavior compared to Rb_2CO_3 on oxides. Mg-Al does not exhibit earlier onset of CH_4 conversion than other catalysts. Besides, most of catalysts (Mg-Gd, Mg-Y, Mg-Sm, Mg-Ce, Mg-Sr) exhibit fairly high C_2 yield (6% ~ 9%). In general, oxide supports strongly influence performance of oxide-supported catalysts.

Table 1. Summary information of all studied catalysts, including BET surface area before and after OCM, property-descriptors ($T_{dec,\ 1st\ CO2}$, $T_{dec,\ last\ CO2}$, $T_{1st\ H2O}$, $T_{last\ H2O}$, $\sigma_{left,\ carb}$ and $\Delta\sigma_{left,\ carb}$) values and performance-descriptors ($Y_{C2,\ 750\ °C}$ and $Y_{C2,\ 800\ °C}$) values.

element combination	Precursor + Support	$metal_{impre}/metal_{sup}$ (mol%)	A_{BET} ($m^2\ g^{-1}$)		Proposed property-descriptors						Performance-descriptors	
					TGA-MS				IR		OCM	
			before OCM	after OCM	$T_{dec,1st\ CO2}$ (°C)	$T_{dec,last\ CO2}$ (°C)	$T_{1st\ H2O}$ (°C)	$T_{last\ H2O}$ (°C)	$\sigma_{left,\ carb}$ (cm^{-1})	$\Delta\sigma_{left,\ carb}$ (cm^{-1})	$Y_{C2,\ 750°C}$ (%)	$Y_{C2,\ 800°C}$ (%)
Rb	pure Rb_2CO_3	n.a.	n.a.	n.a.	926	926	82	82	1435	n.a.	n.a.	n.a.
Rb-Sr	Rb_2CO_3+SrO	10	31.5	24.2	863	863	57	433	1430	-5	1.4	4.4
Rb-Ba	Rb_2CO_3+BaO	10	2.1	23.6	950	950	85	705	1412	-23	0.7	2.9
Rb-Y	Rb_2CO_3+Y_2O_3	10	23.9	21.4	240	912	70	240	1485	50	3.4	7.3
Rb-Ce	Rb_2CO_3+CeO_2	10	21.9	13.2	167	883	167	167	1618	183	0.6	2.9
Rb-Sm	Rb_2CO_3+Sm_2O_3	10	49.8	12	532	892	60	365	1477	42	7.6	10.4
Rb-Gd	Rb_2CO_3+Gd_2O_3	10	31.2	5.6	243	918	96	243	1484	49	2.3	6.2
Rb-Al	Rb_2CO_3+Al_2O_3	10	52.1	57	266	690	85	266	1560	125	3.9	5.8
Cs	pure Cs_2CO_3	n.a.	n.a.	n.a.	892	892	73	130	1422	n.a.	n.a.	n.a.
Cs-Sr	Cs_2CO_3+SrO	10	28.2	61.5	841	841	56	448	1433	11	1.2	3.7
Cs-Ba	Cs_2CO_3+BaO	10	32.2	51.7	1002	1002	95	728	1411	-11	1.0	3.8
Cs-Y	Cs_2CO_3+Y_2O_3	10	16.7	38.8	385	856	76	220	1493	71	3.7	7.2
Cs-Ce	Cs_2CO_3+CeO_2	10	0.5	17.4	151	824	151	151	1615	193	1.0	3.8
Cs-Sm	Cs_2CO_3+Sm_2O_3	10	38.2	14.9	352	826	76	352	1471	49	5.0	8.7
Cs-Gd	Cs_2CO_3+Gd_2O_3	10	22.3	16.9	362	835	73	250	1475	53	4.2	8
Cs-Al	Cs_2CO_3+$A_{l2}O_3$	7	58.2	64.1	201	750	76	201	1497	75	4.3	6.1
Mg	pure $Mg(OAc)_2$	n.a.	n.a.	n.a.	345	345	74	74	1575	n.a.	n.a.	n.a.
Mg-Sr	$Mg(OAc)_2$+SrO	10	35.7	19.8	852	852	67	450	1546	-29	2.3	6.4
Mg-Ba	$Mg(OAc)_2$+BaO	10	16.7	41	995	995	106	620	1565	-10	0.7	2.6
Mg-Y	$Mg(OAc)_2$+Y_2O_3	10	30.4	22.9	325	498	74	325	1563	-12	5.1	8.5
Mg-Ce	$Mg(OAc)_2$+CeO_2	10	14	16.6	315	337	59	337	1565	-10	3.7	6.7
Mg-Sm	$Mg(OAc)_2$+Sm_2O_3	10	28.4	44.3	317	435	71	317	1557	-18	3.9	7.4
Mg-Gd	$Mg(OAc)_2$+Gd_2O_3	10	17.1	17.7	325	510	75	325	1557	-18	6.6	8.7
Mg-Al	$Mg(OAc)_2$+Al_2O_3	8	82.2	67.3	308	355	58	355	1570	-5	1.0	2

Catalyst structure and surface area

The synthesized catalysts were analyzed by different characterization techniques to provide a basis for deriving quantitative property descriptors. Exemplarily SEM-EDX analysis of Rb-based catalyst are shown in SI3. Rb-Y, Rb-Sm and Rb-Gd feature a grain-like morphology that remained apparently unaltered by OCM unlike for Rb-Sr, Rb-Ce, Rb-Ba and Rb-Al where obvious morphological transformations took place. EDX mapping indicates a homogeneous distribution of Rb on a micrometer scale. However, no quantitative descriptors were derived from SEM-EDX.

Table 1 reports the BET surface area values for catalysts before and after OCM testing. For all catalysts the surface area appears to be sufficiently high for OCM catalysis.

XRD was measured on all catalysts before and after OCM. The observed type of crystalline phases, i.e. oxides, hydroxides or carbonates, differ systematically depending on the supported metal and the support oxide. The catalyst supports of Y, Sm and Gd are present as the respective oxide, both before and after OCM. Moreover, no crystalline carbonates were detected on these supports. Also Ce is present as oxide. However, Rb and Cs supported on CeO_2 are present as carbonate before OCM, with Cs_2CO_3 being detected also after OCM. The support oxides SrO and BaO are commonly known for their ability to form very stable carbonates. XRD indicates that both Sr and Ba oxides form carbonates and hydroxides already during the catalyst synthesis. Moreover, the carbonate phases are clearly present also after OCM. None of the supported elements (Rb, Cs, Mg)

was detected as crystalline carbonate on either SrO or BaO. In contrast, alumina showed the presence of carbonates of Rb before and after OCM, while alumina-supported Cs and Mg formed aluminates during OCM.

The XRD analysis indicates that the behavior of the carbonates in the studied bimetallic combination is highly complex. The supported metals and also some supports can exist as carbonate. The OCM reaction can change the phase composition. However, it should be kept in mind that XRD probes only sufficiently crystalline phases, and that carbonates of low crystallinity are not detected by this method. Since IR and TGA-MS are able to detect also carbonates of low crystallinity, both methods were employed to study the catalysts in more detail.

Carbonate stability assessed via TGA-MS

Considering that the carbonate species may be related to OCM performance, their thermal stability was investigated by TGA-MS for Rb_2CO_3, Cs_2CO_3, $Mg(OAc)_2$ on oxides supports. FT-IR spectra were also recorded for all catalysts before and after OCM in order to gain insight into evolution of the carbonate species. With TGA-MS and IR results, six property-descriptors for catalysts (shown in Table 1) were defined.

Detailed analysis of TGA-MS results is shown in SI5. Herein, Rb_2CO_3 on Y_2O_3, CeO_2 and SrO are presented as examples. Rb_2CO_3-Y_2O_3 (Fig. 1a) shows multi-step mass loss and endothermic heat flows with CO_2 and H_2O evolution, indicating carbonate stepwise decomposition with increase of the temperature. Firstly, the mass loss below 200 °C is mainly due to the loss of adsorbed H_2O species. Secondly, the multi-step mass loss between 200 and 650 °C with CO_2 and H_2O evolution, which can be attributed to the decomposition of some carbonaceous species but most likely not Rb_2CO_3. The rare earth carbonate or basic carbonate hydrate, denoted as $Y(OH)_x(CO_3)_y{\cdot}zH_2O$ in general, is metastable and readily decomposes in this intermediate temperature range [34,35]. The formation of $Y(OH)_x(CO_3)_y{\cdot}zH_2O$ species in fresh catalysts could be on one hand attributed to CO_3^{2-} species transfer from Rb_2CO_3 to Y_2O_3, which was proposed by Dubois et al. [36]. On the other hand, inclusion of H_2O and hydroxyls (OH) in forming crystalline structures may be due to hygroscopicity of Rb_2CO_3 that results in migration of these species to the Y_2O_3 support. The process of $Y(OH)_x(CO_3)_y{\cdot}zH_2O$ decomposition to Y_2O_3 is complete when the mass curve plateau appears around 700 °C. Finally, a mass loss with CO_2 release above 700 °C is attributed to Rb_2CO_3 decomposition.

Rb_2CO_3-CeO_2 (Fig. 1b) possesses a different decomposition behavior. The mass shows an abrupt decrease concomitant with a narrow endothermic peak below 200 °C, and CO_2 and H_2O MS peaks. It is attributed to the decomposition of $Ce(OH)_x(CO_3)_y{\cdot}zH_2O$ with low thermal stability [35] rather than to simply loss of surface-adsorbed CO_2 and H_2O species. The plateau between 200 and 650 °C suggests the above decomposition process is completed and only CeO_2 exists in this intermediate temperature range. A mass loss above 700 °C is attributed to decomposition of Rb_2CO_3.

As shown in Fig. 1c, Rb_2CO_3-SrO exhibits another kind of decomposition behavior. A mass loss below 200 °C results from desorption of weakly adsorbed H_2O species. The mass loss around 450 °C with only H_2O evolution is a result of $Sr(OH)_2$ decomposition which apparently was formed by a reaction of SrO with H_2O during impregnation process. Afterwards, it shows mass loss steps after roughly 800 °C, which could be attributed to the decomposition of Rb_2CO_3 and/or $SrCO_3$.

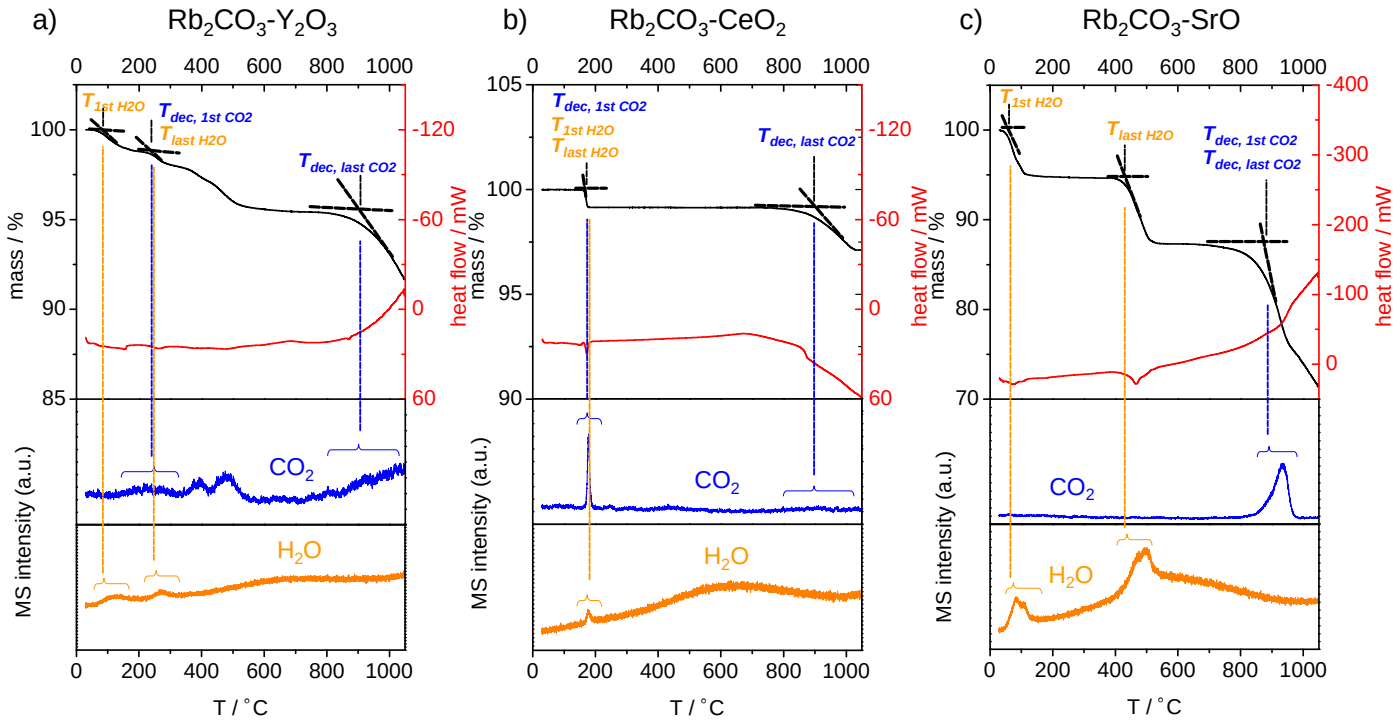

Fig. 1 TGA-MS results of (a) Rb_2CO_3-Y_2O_3, (b) Rb_2CO_3-CeO_2 and (c) Rb_2CO_3-SrO labelled with $T_{dec,\ 1st\ CO2}$ and $T_{dec,\ last\ CO2}$. $T_{dec,\ 1st\ CO2}$ or $T_{dec,\ last\ CO2}$ represents for mass loss temperature when the first or last CO_2 peak appears, respectively. $T_{dec,\ 1st\ CO2}$ and $T_{dec,\ last\ CO2}$ are derived in a universal fashion and labelled in each plot. Rb_2CO_3-Y_2O_3 shows multi-step mass loss and corresponding endothermic heat flows with CO_2 and H_2O evolution, indicating the occurrence of stepwise decomposition dependent on the temperature. Firstly, the mass loss below 200 ℃ is mainly due to adsorbed H_2O species. Secondly, multi-step mass loss between 200 and 650 ℃ can be attributed to decomposition of carbonate hydrate species, which might have been formed through CO_2 transfer from Rb_2CO_3 to Y_2O_3. This process is complete at temperatures when the mass curve plateau appears. Finally, mass loss above 700℃ arises from Rb_2CO_3 decomposition. Differently, Rb_2CO_3-CeO_2 shows an abrupt mass loss and endothermic heat flow below 200 ℃ with apparent CO_2 and H_2O products. This indicates the decomposition of Ce carbonate (or basic carbonate) hydrate with very low thermal stability. Rb_2CO_3-SrO exhibits two obvious mass loss steps (400~500 ℃ and 700~950 ℃) attributed to the decomposition of $Sr(OH)_2$ and $SrCO_3$/Rb_2CO_3, respectively.

The decomposition temperature is employed as a property-descriptor to quantitatively assess carbonate stability between different catalysts. It is derived through the intersection of tangents between the initial and inflection point of the mass loss step [37]. However, only one decomposition temperature descriptor is not sufficient, considering that based on TGA-MS results, there is probably more than one kind of carbonate present in catalysts. Therefore, we propose two different descriptors, $T_{dec,\ 1st\ CO2}$ and $T_{dec,\ last\ CO2}$, representing for carbonate species in catalysts with lowest and highest thermal stability. For example, $T_{dec,\ 1st\ CO2}$ is derived from a mass loss step when the first CO_2 product peak signal appears in MS. It is typically located in a low temperature range. $T_{dec,\ last\ CO2}$ is also derived from a mass loss step but with the last CO_2 peak in MS typically appearing at high temperature range. The above two proposed temperature parameters are both dependent on carbonate species in catalysts. When there are several species present with distinct thermal stability capable of CO_2 evolution, for example, Rb_2CO_3-Y_2O_3 (Fig. 1a) including possibly $Y(OH)_x(CO_3)_y{\cdot}zH_2O$ and Rb_2CO_3, $T_{dec,\ 1st\ CO2}$ and $T_{dec,\ last\ CO2}$ is derived from the respective step and different from each other. Differently, when the two carbonates possess similar thermal stability, such as Rb_2CO_3 and $SrCO_3$ in Rb_2CO_3-SrO (Fig. 1c), there is only one step with significant CO_2 evolution. As a consequence, two descriptors, $T_{dec,\ 1st\ CO2}$ and $T_{dec,\ last\ CO2}$, become identical with each other.

The two descriptors derived through the above approach for each catalyst are summarized in Table 1 and compared in Fig. 2. Based on the above discussion, $T_{dec,\ last\ CO2}$ typically demonstrates the decomposition temperature of carbonates with high stability. As shown in Fig. 2a, Rb_2CO_3 exhibits on most of metal oxide supports a similar decomposition temperature as on

pure Rb_2CO_3. However, Rb_2CO_3-Al_2O_3 shows a much lower decomposition temperature of Rb_2CO_3 than others. A similar difference is also observed for Cs_2CO_3 on oxides (Fig. 2d). This suggests that Al_2O_3 supports facilitate the alkali carbonate decomposition to a much large extent than others. It is the result of the strong polarizing power of Al^{3+} with high charge density. Such behavior is also observed for other Al_2O_3 supported alkali carbonate catalysts in the literature [38].

Differently, $T_{dec,\ 1st\ CO2}$ exhibits significant variation depending on the oxide support. Generally, Rb_2CO_3 and Cs_2CO_3 (especially the latter) on CeO_2 and Al_2O_3 show the lowest $T_{dec,\ 1st\ CO2}$, while on Y_2O_3, Sm_2O_3 and Gd_2O_3 exhibit the intermediate value. In these catalysts, the first CO_2 peak results from the decomposition of the carbonate or hydrocarbonate formed by oxides support through CO_3^{2-} species transfer from alkali carbonate. Their decomposition temperature is much lower than the typical temperature in OCM reaction. Rb_2CO_3 and Cs_2CO_3 on SrO and BaO show the highest $T_{dec,\ 1st\ CO2}$ since all involved carbonates, Rb_2CO_3, Cs_2CO_3, $SrCO_3$ and $BaCO_3$, possess high thermal stability and decompose at around or above OCM reaction temperature.

Unlike Rb_2CO_3 and Cs_2CO_3 on oxides, pure $Mg(OAc)_2$ and $Mg(OAc)_2$ on Y_2O_3, Sm_2O_3 and Gd_2O_3 and CeO_2 exhibit similar $T_{dec,\ 1st\ CO2}$, which can be attributed to decomposition of acetate species. However, $T_{dec,\ 1st\ CO2}$ is much higher for $Mg(OAc)_2$-SrO and $Mg(OAc)_2$-BaO because decomposition of $SrCO_3$ and $BaCO_3$ with higher stability is considered to be the only step to release CO_2 in these two samples (Fig. S5.3f/g). $T_{dec,\ last\ CO2}$ exhibits similar trend to $T_{dec,\ 1st\ CO2}$, while $Mg(OAc)_2$-Y_2O_3, -Sm_2O_3 and -Gd_2O_3 possess distinct values, which correspond the sluggish mass loss with continuous releasing of CO_2 observed at 360 ~ 500 °C (Fig. S5.3b-d). This may indicate the desorption of carbon dioxide from more basic surface sites of MgO such as steps or corners [43].

In summary, the stability of carbonate species present in catalysts can be described in a quantitative fashion by two descriptors, $T_{dec,\ 1st\ CO2}$ and $T_{dec,\ last\ CO2}$. Through comparison, it reveals that the stability of carbonate species present in catalysts is strongly influenced by the oxide support.

Similar to the behavior of CO_2, there is more than one mass loss step releasing H_2O as the product in catalysts based on TGA-MS results. Therefore, we propose two descriptors, $T_{1st\ H2O}$ and $T_{last\ H2O}$, standing for species with earliest and latest H_2O evolution. These two temperature parameters were derived from a similar approach to CO_2-relating descriptors, as shown in Fig. 1. For Rb_2CO_3-Y_2O_3, the first H_2O peak in MS results from the desorption of physisorbed H_2O molecular of samples, which is typically below 100 °C. The last H_2O peak in appears around 200 to 400 °C, possibly attributed to the decomposition of $Y(OH)_x(CO_3)_y{\cdot}zH_2O$ because both H_2O and CO_2 are evolved in this temperature region. Differently, $T_{1st\ H2O}$ and $T_{last\ H2O}$ is identical for Rb_2CO_3-CeO_2, as there is only one significant H_2O peak appearing in MS along with CO_2 simultaneously, suggesting the occurrence of decomposition of $Ce(OH)_x(CO_3)_y{\cdot}zH_2O$. Rb_2CO_3-SrO exhibits another decomposition behavior regarding ~~to~~ H_2O. An obviously sharp peak below 100 °C appears due to the strong hygroscopicity of sample, which is described by $T_{1st\ H2O}$. Afterwards, the dramatic mass loss around 450 °C with substantially greater H_2O peak meanwhile without CO_2 signal ~~is~~ definitely stems from decomposition of $Sr(OH)_2$. Therefore, the H_2O-relating descriptors describe behavior of various species containing physisorbed H_2O, carbonate hydrate and hydroxide in catalysts, which is much more sophisticated than the CO_2-relating descriptors focused only on carbonate species.

$T_{1st\ H2O}$ and $T_{last\ H2O}$ of each catalyst was derived through the above approach and are shown in Table 1 and compared in Fig. 2. In general, $T_{1st\ H2O}$ is typically below 100 °C for all catalysts because it is derived from the desorption of physisorbed H_2O. Differently, $T_{last\ H2O}$ exhibits obvious variation. For Rb_2CO_3-CeO_2 and Cs_2CO_3 -CeO_2, $T_{1st\ H2O}$ comes from decomposition of $Ce(OH)_x(CO_3)_y{\cdot}zH_2O$ below 200 °C. For Rb_2CO_3 and Cs_2CO_3 on Y_2O_3, Sm_2O_3 and Gd_2O_3, $T_{1st\ H2O}$ is also derived from hydroxycarbonate but locates at 200 ~ 400 °C due to different stability of carbonate hydrate. $T_{last\ H2O}$ is also in this temperature range 200 ~ 400 °C for $Mg(OAc)_2$ on CeO_2, Y_2O_3, Sm_2O_3 and Gd_2O_3, but could be mainly attributed to decomposition of $Mg(OAc)_2$. Differently, for Rb_2CO_3, Cs_2CO_3 and $Mg(OAc)_2$ and on SrO and BaO, last H_2O comes from the decomposition of $Sr(OH)_2$ and $Ba(OH)_2$, which typically occurs above 450 °C. Hence, $T_{last\ H2O}$ is more meaningful than $T_{1st\ H2O}$ because it includes the stability information of several species which may be involved in OCM reaction.

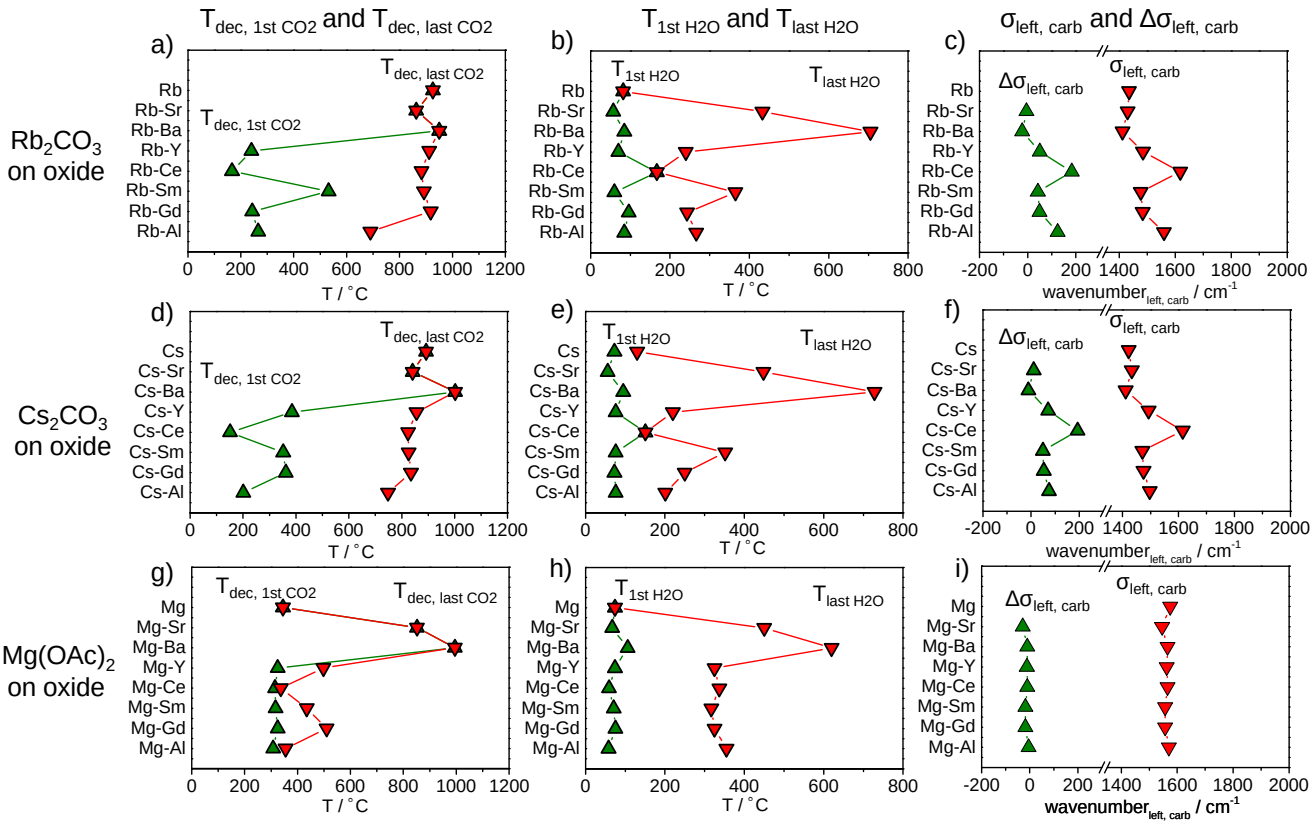

Fig. 2 Derived property-descriptor (a, d, g) $T_{dec, 1st CO2}$ and $T_{dec, last CO2}$, (b, e, h) $T_{1st H2O}$ and $T_{last H2O}$, (c, f, i)$\sigma_{left, carb}$ and $\Delta\sigma_{left, carb}$ for oxide-supported (a - c) Rb_2CO_3 , (d-e) Cs_2CO_3 and (g - h) $Mg(OAc)_2$ as well as values for the respective pure carbonates.

Figure 2a/d/g clearly evidences that for the majority of studied catalysts the most stable carbonate decomposes above 800°C. Hence, the respective carbonate is likely to be present also during OCM catalysis at 800°C. In contrast, all observed hydroxides decompose fully well below 700°C.

Carbonates assessed via IR spectroscopy

IR spectroscopy allows the analysis of carbonates present in the supported catalysts. Fig. 3 depicts exemplarily representative IR spectra obtained before and after OCM catalysis for e.g. a) Rb_2CO_3-Y_2O_3, b) Rb_2CO_3-CeO_2 and c) Rb_2CO_3-SrO as well as d) an illustration how the respective carbonate-related descriptors $\sigma_{left,\ carb}$ and $\Delta\sigma_{left,\ carb}$ were obtained. Rb_2CO_3-Y_2O_3 (Fig. 3a) exhibits absorption peaks in the range of 1700 - 680 cm^{-1}, which can be attributed to the vibrations of CO_3^{2-} species. Specifically, the peak at 1485, 1337 and 1055 cm^{-1} corresponds to asymmetric and symmetric stretching mode of CO_3^{2-}, while the peak at 862 and 714 cm^{-1} is assigned to out-of-plane and in-plane bending mode of CO_3^{2-} [39,40,41,42]. Similar characteristic absorption bands are observed for Rb_2CO_3-CeO_2 (Fig. 3b) and Rb_2CO_3-SrO (Fig. 3c). A whole plot of IR results for all Rb_2CO_3 on oxides catalysts is displayed in Fig. S6.1, where consistent appearance of absorption band in 1700 - 680 cm^{-1} indicates the presence of carbonate species in these fresh catalysts. In addition, the absorption bands in the 3800 - 3000 cm^{-1} region can be assigned to O-H stretching mode of physisorbed H_2O or from hydroxyl groups of hydroxides (identified from XRD patterns). The weak peak around 670 - 500 cm^{-1} is assigned to oxide from the support.

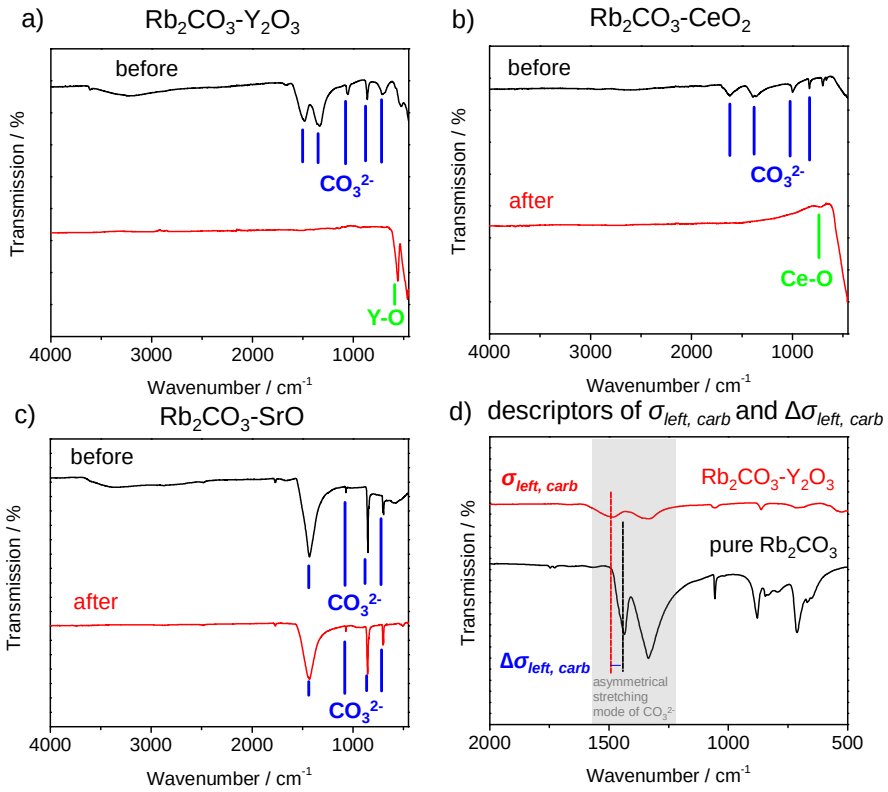

Fig. 3 IR spectra of (a) Rb_2CO_3-Y_2O_3, (b) Rb_2CO_3-CeO_2 and (c) Rb_2CO_3-SrO before and after OCM and (d) definition of descriptors of $\sigma_{left,\ carb}$ and $\Delta\sigma_{left,\ carb}$. For all samples before OCM, the adsorption peaks in the range of 1700 - 650 cm^{-1} were attributed to the vibrations of CO_3^{2-} species. However, for Rb_2CO_3 on Y_2O_3 and CeO_2 catalyst after OCM, characteristic peaks for CO_3^{2-} species significantly reduced while the absorption band corresponding to oxide groups (525 and 664 cm^{-1} for Y-O and Ce-O, respectively) became more pronounced, suggesting the decomposition of CO_3^{2-} species under OCM conditions. Yet, CO_3^{2-} species were still observed for Rb_2CO_3-SrO after OCM due to the high stability of carbonate. The descriptor of $\sigma_{left,\ carb}$ represents the peak position of the left characteristic peak, i.e. highest wave number attributed to asymmetrical stretching mode of CO_3^{2-}. The descriptor $\Delta\sigma_{left,\ carb}$ describes a shift in peak position (wave numbers) between the left characteristic peak for CO_3^{2-} for the oxide-supported carbonate when compared to the corresponding peak in the unsupported pure carbonate sample.

OCM induces characteristic changes in the IR spectra. Firstly, for Rb_2CO_3-Y_2O_3 and Rb_2CO_3-CeO_2 (Fig. 3a/b), the absorption band for CO_3^{2-} species significantly decreases in intensity (or even disappears) while the peak corresponding to oxide groups (525 and 664 cm^{-1} for Y-O and Ce-O, respectively) became more pronounced. This can be attributed to the decomposition of CO_3^{2-} species during OCM reaction because the above carbonate species are not thermodynamically stable at typical OCM temperature and tends to decompose to oxides. Differently, for Rb_2CO_3-SrO (Fig. 3c), signals of CO_3^{2-} species are still clearly observed, although the intensity partially decreases. It reveals the presence of CO_3^{2-} species in catalysts after OCM reaction due to the high stability of $SrCO_3$. Secondly, absorption bands assigned to O-H disappear after OCM, suggesting that hydroxides also decompose during OCM reaction. Hence, the difference before and after OCM with respect to carbonate and hydroxide species is in agreement with the observation of XRD patterns for these samples.

Importantly, the position of the characteristic carbonate peak and its relative shift in oxide-supported catalysts compared to pure carbonate provide the possibility to quantify properties of the carbonate structure and the effect of oxide support. Herein, two property-descriptors, $\sigma_{left,\ carb}$ and $\Delta\sigma_{left,\ carb}$, were defined and derived for all catalysts from IR spectra. In order to simplify and generalize the comparison between different catalysts, the absorption band for asymmetric stretching of C-O bond (1700 - 1400 cm^{-1}) is chosen as the comparative criterion because all catalysts exhibit distinct and strong absorption peak in this range. It is worth mentioning that double peaks appear in this range for most of the measured samples. Herein, the peak on the left of the double peaks, $\sigma_{left,\ carb}$, is defined as one property-descriptor (labelled with red color in Fig. 3d). Compared to pure Rb_2CO_3, oxide-supported Rb_2CO_3 exhibits shift of wave number in IR spectra due to the variation of interaction between CO_3^{2-} and different metal cations. For instance, $\sigma_{left,\ carb}$ of Rb_2CO_3-Y_2O_3 is 1485 cm^{-1} while this value is 1435 cm^{-1} for pure Rb_2CO_3, thus the peak shift is 50 cm^{-1}. Herein, the peak shift, $\Delta\sigma_{left,\ carb}$, is defined as another property-descriptor (labelled with blue color in Fig. 3d) from IR spectra. It indicates the effect of cations in the catalyst support on CO_3^{2-} coordinated with Rb^+, Cs^+ or Mg^{2+}.

The descriptor values of $\sigma_{left,\ carb}$ and $\Delta\sigma_{left,\ carb}$ are shown in Table 1 and compared in Fig. 2. As shown in Fig. 2c, $\sigma_{left,\ carb}$ for Rb_2CO_3-CeO_2, -Y_2O_3, -Sm_2O_3, -Gd_2O_3 and -Al_2O_3 catalysts is higher than the value of pure Rb_2CO_3. This may be attributed to a stronger polarization effect of Ce, Y, Sm, Gd and Al cations on carbonate anion compared to Rb cation, which significantly changes electronic structure of CO_3^{2-} and increases its polarity. Thus, stretching vibration mode of CO_3^{2-} shifts to a higher frequency. But for Rb_2CO_3-SrO and -BaO, no obvious shift can be observed probably because Sr and Ba cations possess similar polarization power relative to Rb cation and cause negligible change to electronic structure of CO_3^{2-}. Fig. 2f depicts the comparison of $\sigma_{left,\ carb}$ for Cs_2CO_3 on oxide catalysts. Qualitatively, the difference in between is similar to the trend obtained from Rb_2CO_3 on oxide catalysts. Differently, $\sigma_{left,\ carb}$ for oxide-supported $Mg(OAc)_2$ catalysts seems to be similar to the value of pure $Mg(OAc)_2$, as shown in Fig. 2i. This suggests that oxide cations cause less impact on acetate species than CO_3^{2-} species probably due because of the different polarizability of acetate.

Correlations between property and performance descriptors

On one hand, oxide-supported catalysts were characterized and property-descriptors were generated from TGA-MS and IR results in order to demonstrate relevant physico-chemical catalyst properties. On the other hand, OCM performance in terms of CH_4 and O_2 conversion as well as C_2 yield was found for all catalysts. Performance-descriptors (C_2 yield) are derived from OCM experiments in order to quantitatively describe catalyst performance at typical OCM temperatures.

Property-performance correlations are established in a quantitative fashion by using property-descriptor as x-axis value and performance-descriptors as y-axis value. In order to evaluate the quality of these property-performance correlations, a preliminary analysis of linear regression is conducted for each proposed correlation to assess the quality of fitting between regression line and experimental data. Residual sum of squares (RSS) is employed as a criterion in comparison of the fitting

regression in a universal fashion. The mathematic definition of RSS is the sum of the square of the vertical deviations from each data point to the fitting regression line, as shown in the followed Equation.

$$RSS = \sum_{i=1}^{n} \left[y_i - \left(a + b\, x_i \right) \right]^2 \quad (1)$$

where *a* and *b* is the intercept and slope value of the linear regression fitting, respectively. This RSS parameter is useful to decide whether the fitted regression line is a good fit or not for the dataset. Generally speaking, the smaller the RSS is, the better obtained regression model fits the data. Two postulations are incorporated into the linear regression fitting. First, the regression line is forced to pass through the data point with highest y-axis value (Rb-Sm). Second, two data subsets are considered – the data points with x-axis values smaller than for Rb-Sm (left region), and the right region of the points with x-axis values larger than for Rb-Sm. For both subsets two separate linear models are obtained. Each regression fitting analysis provides the values RSS_{left} and RSS_{right}, and the sum of both RSS values allows to estimate whether or not the defined property-descriptor is proper to represent a certain catalyst property responsible for OCM performance (Fig. 4).

The diagrams displayed in Figure 4 explores across all catalysts correlations between the C_2 yield measured at 800°C and different physico-chemical property descriptors, i.e. the temperature of the a) first and b) last CO_2 desorption signal in TG-MS, the temperature of c) the first and d) the last H_2O desorption signal, as well as the IR derived descriptors e) $\sigma_{left,\ carb}$ and f) $\Delta\sigma_{left,\ carb}$. Fig. 4a indicates a volcano-like correlation between C_2 yield at 800 °C and $T_{dec,\ 1st\ CO2}$, where C_2 yield increases and then decreases with the increase of $T_{dec,\ 1st\ CO2}$. The trend is also observed when C_2 yield at 750 °C is employed to correlate with $T_{dec,\ 1st\ CO2}$, as shown in Fig. S7.1a. RSS values obtained from linear regression analysis are relatively small for proposed property-performance correlations using $T_{dec,\ 1st\ CO2}$ as property-descriptor, revealing a good quality of fitting between regression line and experimental data. To our knowledge, it is the first time to report a volcano-like correlation between OCM catalytic performance and certain catalysts property (carbonate stability herein) in a quantitative fashion.

For Rb_2CO_3 and Cs_2CO_3 on oxide supports, the latter are able to form carbonates through CO_3^{2-} species transfer from alkali carbonate. This behavior can be also considered as an ability of oxide cations to take CO_3^{2-} species from stable alkali carbonate and subsequently decompose at relatively low temperature. For example, Ce cation captures carbonate species and forms carbonate which decomposes at very low temperature, while C_2 yield over Rb_2CO_3-CeO_2 and Cs_2CO_3-CeO_2 are relatively low~~er~~. Y, Sm and Gd cations tend to form carbonates of intermediate stability and the corresponding catalysts on these supports exhibit higher C_2 yield. Sr and Ba cations are likely to form highly stable carbonates and C_2 yield ~~of~~ over the respective supported catalysts is also relatively low. But for $Mg(OAc)_2$-oxides catalysts, Ce, Y, Sm and Gd cations do not prefer to capture carbonate species and subsequently decompose because $MgCO_3$ itself is easier to decompose due to its lower stability. In contrast, Sr and Ba cations are still able to capture carbonate species and form highly stable forms, which may be related to their high basicity. In addition, $Mg(OAc)_2$-Al_2O_3 seems to be a special case. Mg-Al layered double hydroxides (LDHs) [44,45] may be formed in this case, with some carbonates as main charge-balancing anions and interlayer species. The carbonate species encountered in this substance are beyond the scope of our discussion. Therefore, the performance of $Mg(OAc)_2$-Al_2O_3 could not fit well with the trajectory established on basis of carbonate.

Fig. 4b displays the C_2 yield measured at 800 °C vs. the decomposition temperature of the most stable carbonate species, i.e. $T_{dec,\ last\ CO2}$. Neither here nor for C_2 yields measured at 750 °C a clear correlation is (see also Fig. S7.1b) found. Correspondingly, the respective RSS values are rather high, suggesting that $T_{dec,\ last\ CO2}$ is not a relevant property descriptor.

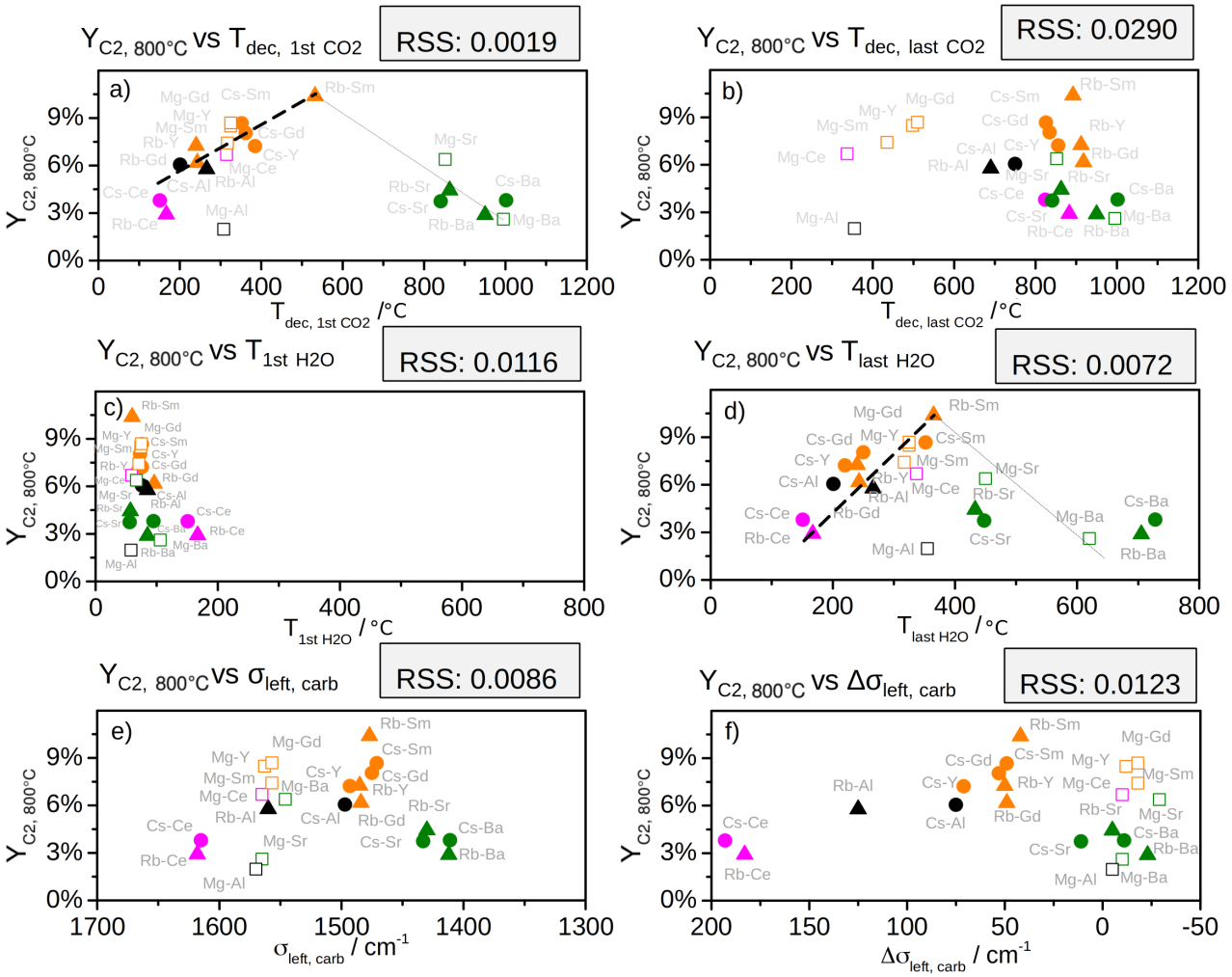

Fig. 4 Correlations between C_2 yield at 800 °C and property-descriptor (a) $T_{dec,\ 1st\ CO2}$, (b) $T_{dec,\ last\ CO2}$, (c) $T_{1st\ H2O}$, (d) $T_{lastH2O}$, (e) $\sigma_{left,\ carb}$ and (f) $\Delta\sigma_{left,\ carb}$ of Rb_2CO_3, Cs_2CO_3 and $Mg(OAc)_2$ on oxides. The provided RSS value (Residual sum of squares) indicates a deviation between fit and experimental values. Lower RSS (a, d) indicate a better fit.

Fig. 4c displays the C_2 yield at 800 °C vs. $T_{1st\ H2O}$. Neither here nor for C_2 yield at 750 °C (Fig. S7.1c) a correlation can be deduced. In contrast, Fig. 4d indicates a possible correlation between C_2 yield at 800 °C and the highest temperature of H_2O desorption, $T_{last\ H2O}$. This correlation is similar to the observed trend between C_2 yield and $T_{dec,\ 1st\ CO2}$ (Fig. 4a). Yet, the deviation between fit and experiment (RSS = 0.0072) is about 4 times higher than for of Y_{C2}, 800°C vs. $T_{dec,\ 1st\ CO2}$ (Figure 4a).

For several catalysts $T_{last\ H2O}$ and $T_{dec,\ 1st\ CO2}$, and in particular for rare earth oxide supported carbonates, both parameters show very similar values. For example for Rb_2CO_3-Y_2O_3 (Fig. 1a) a mass loss step from 200 to 300 °C is observed when H_2O and CO_2 are desorbed simultaneously from the sample, which is in agreement with the previous report of yttrium carbonate hydrate thermolysis [46]. In many cases the carbonate species of lower stability ($T_{dec,\ 1st\ CO2}$) might thus relate to a hydroxy-carbonate.

Potential correlations were also explored between C_2 yield at 800 °C and the IR-derived descriptors $\sigma_{left,\ carb}$ (Fig. 4e) as well as $\Delta\sigma_{left,\ carb}$. (Fig. 4f). Yet, no clear correlation becomes apparent and RSS values remain high. One possible reason could be that Ir spectra were obtained on fresh catalysts and in general a low sensitivity of the IR peak position towards the nature of the carbonates [47].

Discussion and mechanistic interpretation

The descriptor of simple elemental composition is not sufficient to explain the complexity of the catalytic OCM reaction. Herein, property-descriptors about physico-chemical properties of catalysts are introduced and consistently derived from characterization results (TGA-MS and FT-IR). Based on the comparison of RSS values, we conclude that descriptors derived from TGA-MS related to CO_2 desorption and water desorption correlate with C_2 yields measured at 750°C and 800°C, with Y_{CO2} vs. $T_{dec,\ 1st\ CO2}$ showing the best correlation.

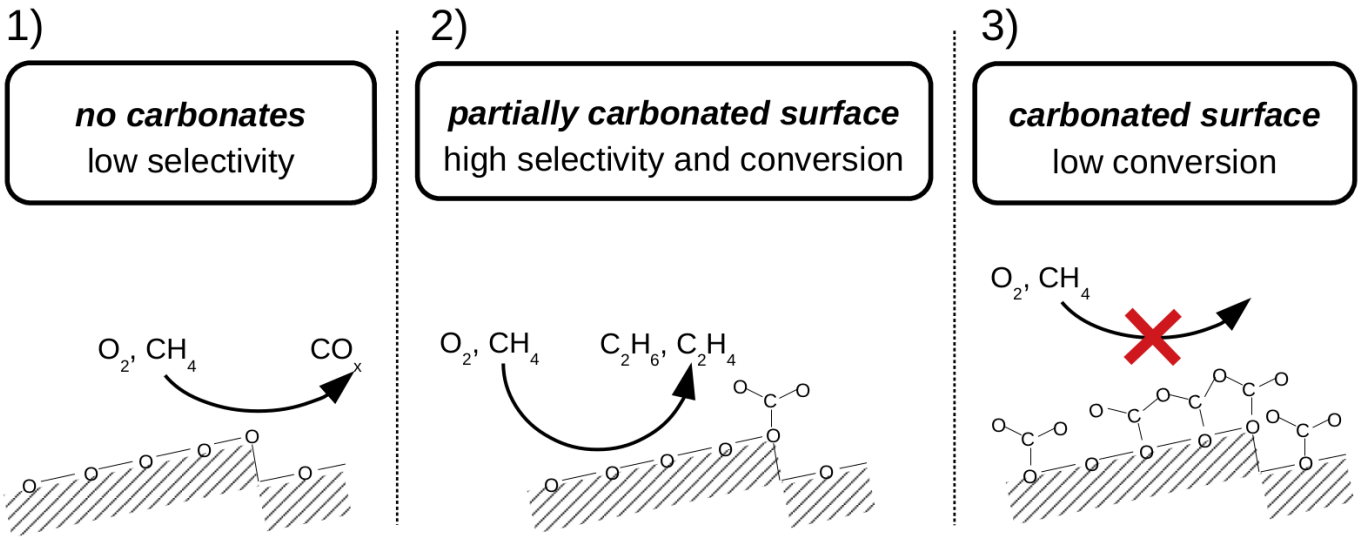

Fig. 5 Possible OCM reaction scheme. Pathways in three surface structural models for oxide-supported carbonate with different stability: 1) ~~no carbonates on~~ carbonates-free surface favors total oxidation with low C_2 selectivity; 2) partial decomposition of carbonates leaves most active (low-coordinated) sites still occupied whereas more selective sites are open to OCM feed affording high conversion and C_2 selectivity; 3) surface (almost) fully covered with highly stable carbonate could not generate active oxygen species to activate CH_4 ~~and~~ resulting in low conversion. Dashed area shows catalyst's surface.

We propose a mechanistic interpretation of the observed behavior as illustrated in Figure 5. The interpretation distinguishes three different states of the catalyst surface during OCM corresponding to either low (Fig. 5.1), medium (Fig. 5.2) or high carbonate stability (Fig. 5.3).

For a low thermal stability (Fig. 5.1) no carbonate species would be presented at OCM temperatures, which leads to the surface composed of oxide exposed to OCM feed. In this situation total oxidation appears to be the favored reaction. MgO-based catalysts can be taken as an example since magnesium oxide is one of the products of $Mg(OAc)_2$ decomposition. It was shown that carbon dioxide adsorption energies and, thus, formation energies of surface carbonates have high values on low-coordinated sites (steps, corners, etc.) [43]. The strongest binding of single CO_2 molecules occurs on step sites with reported adsorption energy about 2.54 eV. This value is equivalent to a desorption temperature of roughly 800 °C assuming thermodynamic equilibrium at $p(CO_2)$ = 1 bar [49]. CO_2 partial pressures are much lower during OCM, hence no carbonates will be present even on low-coordinated sites. These low-coordinated sites are active in methane activation [43,50] facilitating its dissociation. Also they are active in the activation of oxygen [51,52]. In this situation, the chemisorbed fragments of methane molecule (methyl groups) will undergo the full oxidation by activated nearby oxygen species. Hence, CO_x formation would dominate over selective production of C_2 hydrocarbons. The low level of C_2 yield in the left region of volcano plot Figure 4a would then be a consequence of low carbonate stability.

The proposed regime of very stable carbonate species is illustrated in Fig. 5.3. A strongly adsorbed layer of CO_2 or surface carbonate is assumed to cover the catalyst surface even at OCM temperatures. Contrary to materials located on the left leg of the volcano, which mostly feature at least two distinct CO_2 desorption peaks, materials located on the far right of the volcano feature only one CO_2 desorption peak, i.e. only carbonate species. These species require well above 800°C to decompose. These stable surface carbonates obstruct adsorption and activation of CH_4 and O_2, hence their activation cannot proceed. In the right region of volcano the correlation thus might relate to a too strong adsorption of CO_2.

The region near the top of the volcano corresponds to the situation of intermediate carbonate stability (Fig. 5.2). It is only sparsely populated, featuring the element combinations Rb-Sm, Cs-Sm, Cs-Gd, Mg-Gd and Mg-Y. For all of those catalysts two different carbonate decomposition peaks are observed in the TGA experiment (Table 1) implying two types of carbonates. One sort of these carbonates covers unselective (low-coordinated) sites at OCM conditions. The other less stable type is decomposed below reaction temperature, delivering sites for selective oxidation. At the same time, relatively small portion of the surface area covered with carbonates (as follows from trace amounts of CO_3^{2-} for Rb-Sm after OCM reaction, Fig. S6.1c) implying that most of the surface is open for OCM feed providing high conversion rates.

Carbonates can interfere with the mechanism of OCM in different ways. A thin layer of the stable carbonate species could be present at the surface during OCM. Recent temperature-programmed OCM reaction studies of Thum et al. on CaO showed that carbonate phases can be present at reaction conditions and start to decompose at ~750 °C [31]. Also IR spectra obtained after OCM for materials lying on the top of volcano (Rb_2CO_3-Sm_2O_3) indicate the presence of small amounts of carbonates after OCM exposure (Fig. S6.1c). However, the amount of surface carbonate depends on the partial pressure of CO_2, which under reaction conditions can be higher than during post-OCM treatment. Thus, at reaction conditions surface carbonates could be presented in larger amounts.

The less stable carbonate species are likely to be decomposed under OCM conditions, leaving parts of the surface covered with the more stable carbonate. This stable carbonate is likely to be located on the low-coordinated sites, i.e. blocking sites that lead preferentially to methane total oxidation. The remaining oxide surface would still be available for oxygen activation and selective methane conversion. A balance between these two factors, i.e. availability of active sites and blocking of non-selective sites via carbonate formation could be the key factor for selective methane conversion at sufficiently high rates.

We note that proposed mechanistic interpretation describes observed phenomena semiqualitaitvely. For more detailed study further experimental (operando Raman) or theoretical (DFT with CO_2-covered OCM catalyst surfaces) investigations will be needed.

Conclusion

Catalysts composed of alkali metal carbonate or alkaline earth metal carbonate and rare-earth metal oxide or alkaline-earth metal oxide supports were synthesized and their morphology, elemental distribution, crystal phase composition, chemical species, surface area and carbonate stability were characterized. Property-descriptors, $T_{dec,\ 1st\ CO2}$, $T_{dec,\ last\ CO2}$, $T_{1st\ H2O}$, $T_{last\ H2O}$, $\sigma_{left,\ carb}$ and $\Delta\sigma_{left,\ carb}$, were defined and generated on the basis of TGA-MS and IR characterization results. Proven by TGA-MS, more than one kind of carbonate species with different thermal stability are present in oxide-supported carbonate catalysts. Catalytic performance of all catalysts is strongly influenced by oxide supports. Performance-descriptors, $Y_{C2,\ 800\ °C}$ and $Y_{C2,\ 750\ °C}$, were derived from OCM catalytic experiemnts. A volcano-like correlation was observed when using the best property-descriptor, $T_{dec,\ 1st\ CO2}$, representing for stability of carbonate species in catalysts, because it reflects certain chemical reactivity related to OCM reaction and is involved in the proposed mechanism. At the same time supporting materials stay stable under reaction. It is the first time to report a quantitative and convincible correlation between C_2 yield and structural property of OCM catalyst. The isolated sites covered by carbonates suppress total oxidation of methane on the oxide. We conclude that the presence of small amounts of surface carbonates during the reaction is critical for a well-performing OCM catalyst. Catalysts optimization with the concept of carbonate stability could lead to further enhancement of OCM catalytic performance in the future.

Acknowledgement

Huan Wang, Roman Schmack and Ralph Kraehnert acknowledge financial support by the Berlin Graduate school of Natural Sciences and Engineering (BIG-NSE) and the DFG Cluster of Excellence UNICAT (EXC 314).

Method section

Catalysts synthesis. The commercial metal oxides, Y_2O_3, Sm_2O_3, Gd_2O_3 and CeO_2 were purchased from ChemPUR Company in the form of 1mm pellets. These pellets were crushed and sieved to the 224 - 500 µm fraction. SrO and BaO (fine powder, -100 mesh) were obtained from Alfa Aesar. These powders were pressed into tablets, followed by crushing and sieving to the 224 - 500 µm fraction as well. All obtained metal oxides were treated at 800 °C in air for 2 h before using as the support for impregnation. The calcination was done for all supports in order to insure their stability under OCM reaction conditions in contrast to stability of carbonates.

Catalysts containing alkali carbonate (Rb_2CO_3 and Cs_2CO_3) or alkaline earth acetate (Mg acetate) and metal oxide supports were prepared via a dropwise impregnation in a self-made apparatus [33]. Considering that $MgCO_3$ is not sufficiently soluble for aqueous solution impregnation, $Mg(OAc)_2$ was used as a water soluble Mg precursor. The apparatus is composed of a syringe pump and a rotary evaporator with controlled vacuum. The ratio of impregnated metal element to the metal element of oxide support was 10 mol% and was kept the same for all prepared catalysts, supported and precursors in our study. Typically, 1.0 g of Y_2O_3 granules were placed into a 100 mL flask and preheated for 15 min in a water bath to 72 °C with rotation at 50 rpm. 102.3 mg Rb_2CO_3 (Aldrich, 99.8%) was dissolved in 10 mL milli-Q H_2O. The Rb_2CO_3 solution was continuously dosed to the Y_2O_3 in the rotary evaporator (80 mbar) via syringe pump at a rate of 1.7 mL/h. The material was then dried in vacuum oven at 150 °C for 5 h. No further heat treatment was applied.

The commercial carbonate $SrCO_3$ was purchased from Alfa Aesar Company in the form of powder. This powder was pressed into tablets, crushed and sieved into size fraction from 224 to 500 µm. The obtained material was treated in vacuum oven at 150 °C for 5 h to remove water and other residues. Afterwards, the treated material was used as support for the following impregnation.

Catalysts were prepared through drop-wise impregnation of Rb_2CO_3 and Cs_2CO_3 aqueous solution on above carbonate supports (similar to the preparation process for oxide-supported catalysts). For all prepared catalysts, the molar ratio of impregnated metal element to the metal element of carbonate support is 10 mol%.

Rb_2CO_3, Cs_2CO_3 and $Mg(OAc)_2$ supported on Al_2O_3 were synthesized via impregnation of the respective precursor onto alumina as described elsewhere [53]. The employed γ-Al_2O_3 support was supplied by Südchemie/Clariant as "Al_2O_3-100" pellets, which were ground and sieved to a size fraction of 200 - 500 µm. Thereafter, the Al_2O_3 was calcined for 12 h at 800 °C in air. The support was then loaded via wet impregnation with aqueous solutions and dried. Catalyst loading was chosen as 23.1 wt% of the employed salts in anhydrous state. Drying conditions for Cs_2CO_3 were 1 h at 60 °C and 60 mbar, followed by 5 min at 60 °C and 30 mbar using a rotary evaporator. For Rb_2CO_3 and $Mg(OAc)_2$ – 30 min at 60 °C and 60 mbar.

Catalyst characterization. Scanning electron microscopy (SEM) images of catalysts were recorded on a JEOL 7401F instrument at 10 kV acceleration voltage and 8 mm working distance. Energy dispersive X-ray spectroscopy (EDX) mapping was performed on the same instrument with Bruker Quantax EDX detector at 12 kV acceleration voltage and 12 mm working distance. X-ray powder diffraction (XRD) was measured using a Bruker D8 advanced powder diffractometer in Bragg-Brentano geometry (CuKα source, λ = 0.15405 nm), variable divergence slit and a position sensitive LynxEye detector. FTIR spectra were recorded in the range between 4000 and 450 cm-1 on a Perkin Elmer Spectrum 100 on samples without pressing in KBr. The Quantachrome Autosorb-1 was used for the physisorption test. The samples were treated at 150 °C overnight before the measurement at 77K. BET method for relative pressure p/p0 in the appropriate range was used to determine specific surface area. Thermogravimetric analysis (TGA) was performed on a PerkinElmer STA 8000. For each measurement approximately 40 mg of the sample was heated in argon (60 mL min-1) from 30 °C to 1050 °C with ramping rate of 5 K min-1. The gas-phase products evolved during heating were monitored by a PerkinElmer Clarus SQ8 GC-MS mass spectrometer [54].

Catalytic testing in OCM. Activity of the catalysts was tested in a reactor system developed at the Leibniz Institute for Catalysis. This system consists of 6 continuous-flow fixed-bed reactors quartz tubular (internal diameter = 6 mm) reactors located in the same oven and operating in parallel. 50 mg catalyst (size fraction 224-500 µm) was placed on a quartz wool plug covered with roughly 700 mg SiC particles to ensure proper heat transfer. The feed gas was continuously dosed at a composition of CH4/O2/N2 ~ 26%/15%/59% with a total gas flow rate of 102.2 mLSTP min-1. This flow was equally distributed to the reactors filled with catalysts. They were initially heated in the feed gas to 450°C. Thereafter, the temperature was increased in steps of 25 K from 450 °C to 800 °C. An online gas chromatograph (Agilent 7890) was used for quantifying O2, N2, CO, and CO2 with a thermal conductivity detector (TCD) and CH4, C2H4, C2H6 with a flame ionization detector (FID). N2 was used as internal standard. Two GC test rounds were performed at each temperature. At the highest temperature (800°C), three GC test rounds were measured to provide indication of the catalyst stability. After OCM tests, the reactors were cooled down to room temperature in the feed gas. OCM performance of catalysts on Al2O3 support was tested by utilizing identical amount of catalysts, feed composition, flow rate per channel and reaction temperature range.

The feed conversion was calculated from the inlet and outlet molar ($\acute{n}$) flow, e.g. CH_4 conversion (X_{CH4}) and O_2 conversion (X_{O2}) according to Equation 2 and 3. The desired reaction products of OCM are C_2H_4 and C_2H_6. Their overall yield (Y_{C2}) is written in Equation 4. Selectivity of C_2H_4 and C_2H_6 was calculated by Y_{C2} and X_{CH4} in Equation 5.

$$X_{CH_4} = \frac{\acute{n}_{CH_4,inlet} - \acute{n}_{CH_4,outlet}}{\acute{n}_{CH_4,inlet}} \quad (2)$$

$$X_{O2} = \frac{\acute{n}_{O2,inlet} - \acute{n}_{O2,outlet}}{\acute{n}_{O2,inlet}} \quad (3)$$

$$Y_{C_2} = \frac{2 * \acute{n}_{C_2H_4,outlet} + 2 * \acute{n}_{C_2H_6,outlet}}{\acute{n}_{CH_4,inlet}} \quad (4)$$

$$S_{C_2} = \frac{Y_{C2}}{X_{CH4}} \quad (5)$$

Supporting Information

This information is available free of charge on the ACS Publications website.

SI1 Basicity concepts in OCM catalysis
SI2 Measured OCM performance
SI3 Catalyst morphology and element distribution (SEM-EDX)
SI4 Crystalline phases (XRD)
SI5 Measuring potential descriptors
SI6 IR spectra
SI7 Correlations between catalyst properties and OCM performance

References

1. A. Holmen. Direct conversion of methane to fuels and chemicals. Catalysis Today 142 (2009) 2-8.
2. R. Horn, R. Schlögl. Methane activation by heterogeneous catalysis. Catalysis Letters 145 (2015) 23-39.
3. C. Mesters. A selection of recent advances in C1 chemistry. Annual Review of Chemical and Biomolecular Engineering 7 (2016) 223-238.
4. P. Schwach, X. Pan, X. Bao. Direct conversion of methane to value-added chemicals over heterogeneous catalysts: challenges and prospects. Chemical Review 117 (2017) 8497-8520.
5. E.V. Kondratenko, T. Peppel, D. Seeburg, V.A. Kondratenko, N. Kalevaru, A. Martin, S. Wohlrab. Methane conversion into different hydrocarbons or oxygenates: current status and future perspectives in catalyst development and reactor operation. Catalysis Science & Technology 7 (2017) 366-381.
6. E.V. Kondratenko, M. Baerns, Nanostructured Catalysts: Selective Oxidations, The Royal Society of Chemistry, 2011, pp. 35-55.
7. E.V. Kondratenko, U. Rodemerck, in: P. Granger, V.I. Parvulescu, S. Kaliaguine, W. Prellier (Eds.), Perovskites and Related Mixed Oxides, Wiley-VCH Verlag GmbH & Co. KGaA, Weinheim, 2016, p. 517.
8. Y.S. Su, J.Y. Ying, W.H. Green Jr. Upper bound on the yield for oxidative coupling of methane. Journal of Catalysis 218 (2003) 321-333.
9. G.E. Keller, M.M. Bhasin. Synthesis of ethylene via oxidative coupling of methane: I. Determination of active catalysts. Journal of Catalysis 73 (1982) 9-19.
10. R. Schlögl. Heterogeneous catalysis. Angewandte Chemie Int. Ed. 54 (2015) 3465–3520.
11. Y. Simon, F. Baronnet, G. M. Côme, et al., in Studies in Surface Science and Catalysis, Vol. 147, Elsevier, 2004, pp. 571.
12. E.-J. Ras, G. Rothenberg. Heterogeneous catalyst discovery using 21st century tools: a tutorial. RSC Advances 4 (2014) 5963-5974 .
13. V.I. Lomonosov, M.Yu. Sinev. Oxidative coupling of methane: Mechanism and kinetics. Kinetics and Catalysis, 57 (2016) 647–676.
14. A.I. Olivos-Suarez, À. Szécsényi, E.J.M. Hensen, J. Ruiz-Martinez, E.A. Pidko, J. Gascon. Strategies for the direct catalytic valorization of methane using heterogeneous catalysis: challenges and opportunities. ACS Catalysis 6 (2016) 2965.
15. J.A.S.P. Carreiro, M. Baerns. Oxidative coupling of methane: II. Composite catalysts of basic materials. Journal of Catalysis 117 (1989) 396-403.
16. V.R. Choudhary, S.A.R. Mulla, B.S. Uphade. Oxidative coupling of methane over alkaline earth oxides deposited on commercial support precoated with rare earth oxides. Fuel 78 (1999) 427-437.
17. V.R. Choudhary, V.H. Rane, R.V. Gadre. Influence of precursors used in preparation of MgO on its surface properties and catalytic activity in oxidative coupling of methane. Journal of Catalysis 145 (1994) 300-311.
18. V.R. Choudhary, V.H. Rane, M.Y. Pandit. Comparison of alkali metal promoted MgO catalysts for their surface acidity/basicity and catalytic activity/selectivity in the oxidative coupling of methane. Journal of Chemical Technology & Biotechnology 68 (1997) 177-186.
19. A.M. Maitra, I. Campbell, R.J. Tyler. Influence of basicity on the catalytic activity for oxidative coupling of methane. Applied Catalysis A: General 85 (1992) 27-46.
20. V.D. Sokolovskii, S.M. Aliev, O.V. Buyevskaya, A.A. Davydov. Type of hydrocarbon activation and nature of active sites of base catalysts in methane oxidative dehydrodimerization. Catalysis Today 4 (1989) 293-300.
21. D.W. Smith, An acidity scale for binary oxides, Journal of Chemical Education, 64 (1987) 480.
22. J.A. Duffy, A review of optical basicity and its applications to oxidic systems, Geochimica et Cosmochimica Acta, 57 (1993) 3961-3970.
23. A. Lebouteiller and P. Courtine, Improvement of a bulk optical basicity table for oxidic systems, Journal of Solid State Chemistry, 137 (1998) 94-103.
24. U. Zavyalova, M. Holena, R. Schlögl, M. Baerns. Statistical analysis of past catalytic data on oxidative methane coupling for new insights into the composition of high-performance catalysts. ChemCatChem 3 (2011) 1935-1947.
25. L. Pirro, P.S.F. Mendes, S. Paret, B.D. Vandegehuchte, G.B. Marin, J.W. Thybaut. Descriptor–property relationships in heterogeneous catalysis: exploiting synergies between statistics and fundamental kinetic modelling Catalysis Science & Technology 9 (2019) 3109.

26. G. Kumar, S.L.J. Lau, M.D. Krcha, M.J. Janik. Correlation of methane activation and oxide catalyst reducibility and its implications for oxidative coupling. ACS Catalysis 6 (2016) 1812−1821.
27. S. Lim, J.-W. Choi, D.J. Suh, K.H. Song, H.C. Ham, J.-M. Ha. Combined experimental and density functional theory (DFT) studies on the catalyst design for the oxidative coupling of methane. Journal of Catalysis 375 (2019) 478−492.
28. J. Ohyama, T. Kinoshita, E. Funada, H. Yoshida, M. Machida, S. Nishimura, T. Uno, J. Fujima, I. Miyazato, L. Takahashi, K. Takahashi. Direct design of active catalysts for low temperature oxidative coupling of methane via machine learning and data mining. Catalysis Science & Technology 11 (2021) 524-530.
29. R. Schmack, A. Friedrich, E.V. Kondratenko, J. Polte, A. Werwatz, R. Kraehnert. A meta-analysis of catalytic literature data reveals property-performance correlations for the OCM reaction. Nature Communications 10 (2019) 441.
30. Y. Xu, L. Yu, C. Cai, J. Huang, X. Guo. A study of the oxidative coupling of methane over SrO-La2O3/CaO catalysts by using CO2 as a probe. Catalysis Letters 35 (1995) 215−231.
31. L. Thum, M. Rudolph, R. Schomäcker, Y. Wang, A. Tarasov, A. Trunschke, R. Schlögl. Oxygen Activation in Oxidative Coupling of Methane on Calcium Oxide. Journal of Physical Chemistry C 123 (2019) 8018-8026.
32. C. Estruch Bosch, M.P. Copley, T. Eralp, E. Bilbé, J.W. Thybaut, G.B. Marin, P.Collier. Tailoring the physical and catalytic properties of lanthanum oxycarbonate nanoparticles. Applied Catalysis A: General 536 (2017) 104-112.
33. H. Wang, R. Schmack, B. Paul, M. Albrecht, S. Sokolov, S. Rümmler, E.V. Kondratenko, R. Kraehnert. Porous silicon carbide as a support for Mn/Na/W/SiC catalyst in the oxidative coupling of methane. Applied Catalysis A: General 537 (2017) 33-39.
34. R.G. Charles. Rare-earth carbonates prepared by homogeneous precipitation. Journal of Inorganic and Nuclear Chemistry 27 (1965) 1489-1493.
35. L.M. D'Assunção, I. Giolito, M. Ionashiro. Thermal decomposition of the hydrated basic carbonates of lanthanides and yttrium. Thermochimica Acta 137 (1989) 319-330.
36. J.-L. Dubois, C.J. Cameron. Synergy between stable carbonates and yttria in selective catalytic oxidation of methane. Chemistry Letters 20 (1991) 1089-1092.
37. A.A. Askadskii, Computational Materials Science of Polymers. Cambridge International Science Publishing Ltd. (2003).
38. W.H.J. Stork, G.T. Pott. Studies of compound formation on alkali/. gamma.-aluminum oxide catalyst systems using chromium, iron, and manganese luminescence. Journal of Physical Chemistry 78 (1974) 2496-2506.
39. M.A. Alavi, A. Morsali. Syntheses and characterization of Sr(OH)2 and SrCO3 nanostructures by ultrasonic method Ultrasonics Sonochemistry 17 (2010) 132-138.
40. B. Eckhardt, E. Ortel, D. Bernsmeier, J. Polte, P. Strasser, U. Vainio, F. Emmerling, R. Kraehnert. Micelle-templated oxides and carbonates of zinc, cobalt, and aluminum and a generalized strategy for their synthesis. Chemistry of Materials 25 (2013) 2749-2758.
41. T. Mokkelbost, I. Kaus, T. Grande, M.-A. Einarsrud. Combustion Synthesis and Characterization of Nanocrystalline CeO2-Based Powders. Chemistry of Materials 16 (2004) 5489-5494.
42. M. Rahimi-Nasrabadi, S.M. Pourmortazavi, M. Aghazadeh, M.R. Ganjali, M. Sadeghpour Karimi, P. Novrouzi. Samarium carbonate and samarium oxide; synthesis, characterization and evaluation of the photo-catalytic behavior. Journal of Materials Science: Materials in Electronics 28 (2017) 5574-5583.
43. A. Mazheika, S.V. Levchenko. Ni Substitutional Defects in bulk and at the (001) surface of MgO from first-principles calculations. Journal of Physical Chemistry C 120 (2016) 26934-26944.
44. A. Vaccari. Preparation and catalytic properties of cationic and anionic clays. Catalysis Today 41 (1998) 53-71.
45. J.S. Valente, G. Rodriguez-Gattorno, M. Valle-Orta, E. Torres-Garcia. Thermal decomposition kinetics of MgAl layered double hydroxides. Materials Chemistry and Physics 133 (2012) 621-629
46. P.P. Fedorov, N.V. Il'in. Yttrium carbonate thermolysis. Russian Journal of Inorganic Chemistry 57 (2012) 237-241.
47. G. Busca, V. Lorenzelli. Infrared spectroscopic identification of species arising from reactive adsorption of carbon oxides on metal oxide surfaces. Materials Chemistry 7 (1982) 89-126.
48. J.L. Callahan, R.K. Grasselli. A selectivity factor in vapor-phase hydrocarbon oxidation catalysis. AIChE Journal 9 (1963) 755-760.
49. D. Stull, H. Prophet, JANAF Thermochemical Tables, 2nd edn. U.S. National Bureau of Standards, Washington, D.C., 1971.
50. P. Schwach, N. Hamilton, M. Eichelbaum, L. Thum, T. Lunkenbein, R. Schlögl, A. Trunschke. Structure sensitivity of the oxidative activation of methane over MgO model catalysts: II. Nature of active sites and reaction mechanism. Journal of Catalysis 329 (2015) 574−587.
51. S. Bhattacharya, D. Berger, K. Reuter, L.M. Ghiringhelli, S.V. Levchenko. Theoretical evidence for unexpected O-rich phases at corners of MgO surfaces. Phys. Rev. M 1 (2017) 071601.

52. S. Bhattacharya, S.V. Levchenko, L.M. Ghiringhelli, M. Scheffler. Stability and metastability of clusters in a reactive atmosphere: theoretical evidence for unexpected stoichiometries of Mg_MO_x. Phys. Rev. Lett. 111 (2013) 135501.
53. M. Kusche, F. Enzenberger, S. Bajus, H. Niedermeyer, A. Bösmann, A. Kaftan, M. Laurin, J. Libuda, P. Wasserscheid. Enhanced activity and selectivity in catalytic methanol steam reforming by basic alkali metal salt coatings. Angewandte Chemie Int. Ed. 52 (2013) 5028–5032.
54. E.V. Kondratenko, M. Schluter, M. Baerns, D. Linke, M. Holena. Developing catalytic materials for the oxidative coupling of methane through statistical analysis of literature data. Catalysis Science & Technology, 5 (2015) 1668–1677.